

Kuijun Zuo¹, Xianxu Yuan², Weiwei Zhang¹ & Zhengyin Ye¹

¹School of Aeronautics, Northwestern Polytechnical University, Xi'an, 710072, China ²State Key Laboratory of Aerodynamics, China Aerodynamics Research and Development Center, Mian'yang, 621000, China

Abstract

The computation of aerodynamic parameters using Navier-Stokes (NS) equations is notably time-consuming. To address this, a data-driven Deep Attention Network (DAN) is introduced for rapid reconstruction of steady flow fields over various airfoil shapes. To effectively represent geometric information of different airfoils, the airfoil profile grayscale images fed into the network are segmented into distinct patches, and embedding corresponding positional information. Subsequently, these embedded geometric vectors are processed through a Transformer encoder to extract attention-based geometric features specific to each airfoil. Finally, the extracted geometric features from the Transformer encoder, combined with flow coordinates and wall distance, are fused and input into a multi-layer perceptron to predict the velocity and pressure fields of the airfoil. Through quantitative and qualitative analysis of extensive experimental results, it is observed that the proposed deep attention network model possesses certain geometric interpretability. Furthermore, it showcases robust generalization capabilities and high prediction accuracy across a wide array of airfoil flow fields.

Keywords: Flow field prediction; Deep learning; Self-attention network; Aerodynamics

1. Introduction

In aerodynamics, calculating the flow field is a crucial step to study complex flow phenomena such as flow separation and transition to turbulence. Typically, the airfoil flow field is computed by solving the NS equations on appropriate computational grids. With the advancement of high-performance computing and efficient computational methods, the computational time required for Computational Fluid Dynamics (CFD) simulations has been significantly reduced. Consequently, CFD simulation methods are commonly employed for aerodynamic design and analysis, replacing some experimental investigations. However, for solving large and intricate engineering problems, CFD simulations still demand extensive iterations. Therefore, simulating flows through solving the NS equations remains expensive and time-consuming for such cases. In recent years, the rapid development of machine learning techniques in the field of data science has introduced a new paradigm for modeling physical systems, known as data-driven modeling. Leveraging machine learning enables the analysis and modeling of historical aerodynamic data, accelerating the efficiency of future aerodynamic modeling. Researchers in this domain have made numerous attempts to explore and utilize these techniques. Guo et al. [1] were among the first to employ convolutional neural networks for predicting steady flow fields. Through experiments, researchers found that the velocity field prediction based on convolutional neural networks was two orders of magnitude faster than CFD solvers accelerated by GPUs and four orders of magnitude faster than CPU-based solvers. Cihat Duru et al. [2] established a functional mapping relationship between the Signed Distance Function (SDF) and the pressure field of an airfoil. They utilized convolutional neural networks to train the model, which accelerated the computation speed of the airfoil's pressure field. The Signed Distance Function is widely applied in deep learning flow field modeling due to its capability to deeply characterize geometric features. Saakaar

Bhatnagar et al. [3] used the SDF of an airfoil as the geometric input and predicted the airfoil's velocity and pressure fields as outputs, utilizing a convolutional neural network as the foundational architecture for predicting the airfoil flow field. Similarly, Wu et al. [4] and Ribeiro et al. [5] followed a similar approach, augmenting the neural network inputs with a label channel that reflects initial boundary conditions to characterize the flow field. Additionally, Generative Adversarial Networks (GANs) have found widespread use in the field of flow field prediction. Chen et al. [6] employed airfoil images as inputs, subsequently merging encoded geometric information of the airfoil with Reynolds numbers and angles of attack, decoding them into corresponding flow field outputs. They established a one-to-one mapping relationship between given boundary conditions, geometric shapes, and their respective flow fields. Following a similar network architecture, Wu [7] and Wang et al. [8] conducted related research in this area. Hu et al. [9] successively introduced an improved deep learning flow field prediction model based on the UNet architecture. Their approach differed from previous models by defining the input network parameters from the perspective of grid generation, which enhanced the physical constraints of the modeling to some extent. A common characteristic of the aforementioned methods is the establishment of a mapping between geometry and flow fields, conducting research on the entire flow field. This type of solving method is defined here as a "field-to-field" mode. Once the solving domain is fixed, after training, neural networks can only predict flow fields of the same domain size, limiting their flexibility in solving. In order to obtain more accurate solutions for the nearwall region of the airfoil flow field, Sekar et al. [10] employed a "point-to-point" mode to predict the flow field. Specifically, this method involves two main steps: 1) utilizing a convolutional neural network to extract geometric parameters from the input airfoil image; 2) inputting the geometric parameters obtained in step (1) along with flow characteristic parameters such as Reynolds number and angle of attack into a Multilayer Perceptron (MLP) to predict the flow field at each grid point. Zuo et al. [11] also explored the application of multi-task learning in flow field modeling. Considering step (1), ensuring an equal number of geometric coordinates for different airfoils and necessitating separate training of a convolutional neural model for both geometric extraction and flow field prediction poses several practical challenges. To address this issue, this paper conducts rapid flow field predictions for different airfoils based on the Transformer [12] neural network architecture. Expanding on prior research, this study further delves into augmenting the interpretability of geometric features and enhancing the generalization capability of the DAN model.

The rest of this article is organized as follows. Section II primarily introduces the architecture and hyperparameter design of the self-attention network used for extracting airfoil geometric features, along with the multi-layer perceptron employed for flow field prediction. Section III delineates the definition and division of the flow field dataset. Section IV analyzes the training results of the deep learning model. Section V extensively discusses the flow field prediction results of the deep attention network model. And the conclusion is given in Section VI

2. Constructing the Deep Learning Flow Field Prediction Network

2.1 Airfoil Geometric Feature Extraction Network

In existing literature, convolutional neural networks have been widely used for flow field prediction tasks. However, as the feature dimension increases, deep learning model architectures become more complex, leading to increased training costs. Inspired by the significant success of vision Transformer [13] in image segmentation and recognition fields, here we employ Transformer encoders based on self-attention mechanisms to extract geometric information from different airfoils. As shown in Figure 1, for the Transformer encoder, the initial step involves partitioning the airfoil image $\chi = \mathbb{R}^{H \times W \times C}$ into a series of two-dimensional patches $\chi \in \mathbb{R}^{N \times (E^2.C)}$. Here, $H \times W$ represents the original resolution of the airfoils, C signifies the number of channels in the airfoil image, $E \times E$ denotes the resolution of each airfoil image patch, and $N = HW/E^2$ indicates the total number of airfoil patches. To facilitate subsequent neural network training tasks, the series of two-dimensional patches are further transformed into one-dimensional embeddings. To maintain the positional information of these embeddings within the original airfoil image during neural network training, positional encodings are embedded into the embeddings. Additionally, an extra learnable embedding token is defined to map the geometric features of the airfoil. The calculation formula for positional encoding is:

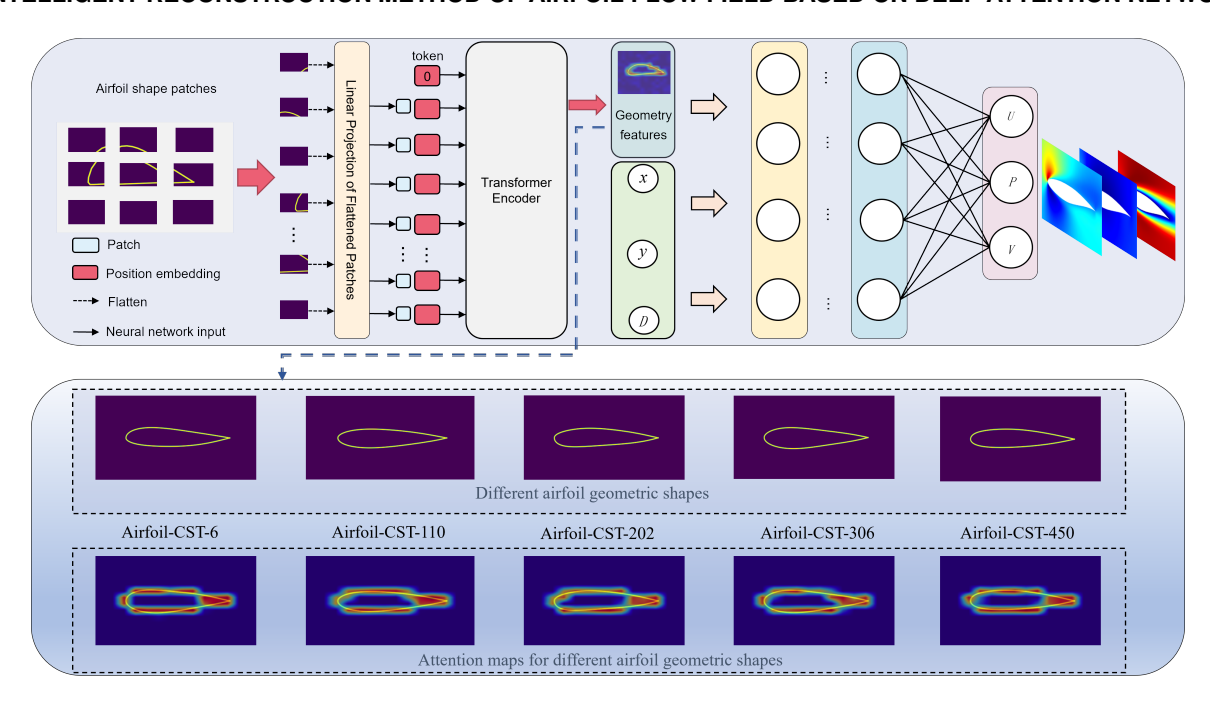


Figure 1 – Deep attention network architecture for flow field prediction.

$$PE(pos, 2i) = \sin\left(pos/10000^{2i/d_{model}}\right)$$

$$PE(pos, 2i + 1) = \cos\left(pos/10000^{2i/model}\right)$$
(1)

The Transformer encoder primarily consists of 12 identical neural network feature extractors. Each module mainly comprises a LayerNorm (LN) layer, a multi-head self-attention layer (MHSA), and a multi-layer perceptron (MLP) layer. As depicted in Figure 2, the multi-head attention layer mainly comprises three parts: queries Q and a series of key-value pairs (K,V) with a dimensionality of d_{model} . The computation involves computing the dot product of Q with all K and then applying the softmax function to obtain the weights for V. The calculation formula is:

$$Attention(Q, K, V) = \operatorname{soft} \max \left(\frac{QK^{T}}{\sqrt{d_k}}\right) V \tag{2}$$

Furthermore, we utilize the multi-head attention network to integrate the geometric features of different patches of the airfoil:

$$\begin{cases} & \text{MultiHead } (Q,K,V) = \text{ Concat } (\text{ head }_1,\ldots,\text{ head }_m) W^E \\ & \text{head }_i = \text{Attention} \left(QW_i^Q,KW_i^K,VW_i^V\right) \end{cases} \tag{3}$$

As shown in Figure 1, when the calculated attention scores are fed back into the original airfoil image, it can be observed that compared to traditional convolutional neural networks and similar models, the geometric features of airfoils extracted by the Transformer network exhibit good geometric interpretability. Moreover, it can effectively extract meaningful boundary feature for different airfoils. This reflects the considerable potential of Transformer network architecture in extracting geometric features from airfoils, indicating promising applications in flow field prediction.

2.2 Flow Field Prediction Network

Figure 3 depicts a typical multi-layer perceptron (MLP) neural network architecture, consisting of three main components: the input layer, hidden layers, and the output layer. The input to the MLP comprises 13 physical parameters. G_i denotes 10 latent airfoil geometric features extracted by the transformer encoder. D_i represents the wall distance at any point in the airfoil flow field. x and y denotes the coordinate information of different positions within the flow field. MLP neural networks have fully connected layers, meaning each neuron in an upper layer is connected to every neuron in

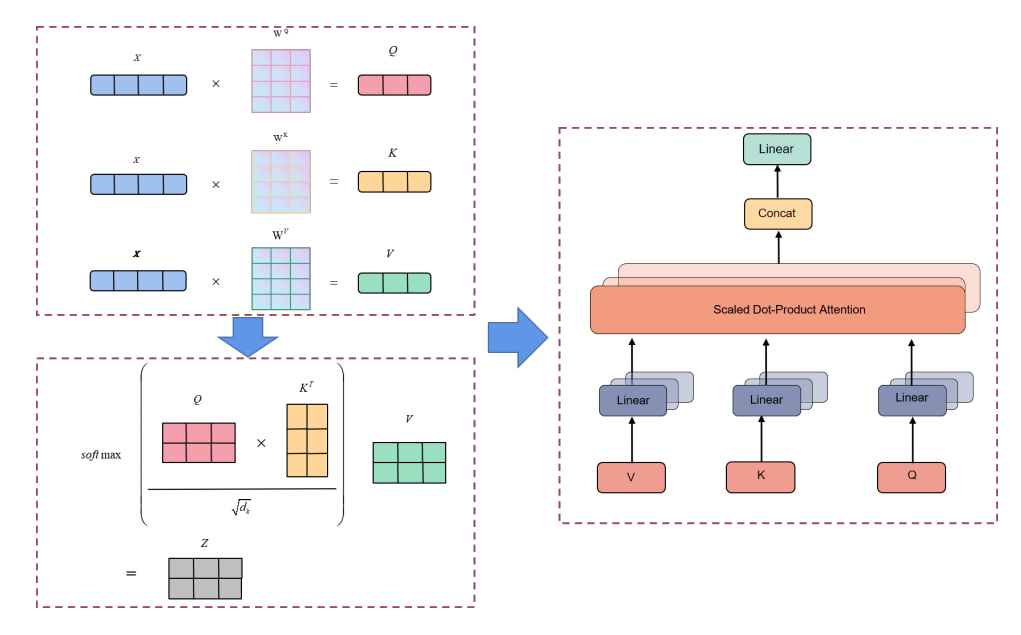


Figure 2 – Multi-head attention layer.

the subsequent layer. There are three fundamental elements in an MLP: weights, biases, and activation functions. The weights are used to control the strength of connections between neurons, and their magnitude indicates the strength of possibility. Biases are crucial parameters within the model, ensuring that the output values computed from input values aren't arbitrarily activated. The activation function plays a role in nonlinear mapping, restricting the range of neuron amplitudes typically to (-1, 1) or (0, 1). The output of the neural network consists of pressure p and the velocity components p and p directions, respectively. The prediction function for the MLP can be defined as follows:

$$f_{MLP}(D_i, x, y, G_i) = (u, v, p) \tag{4}$$

On the left-hand side represents the prediction function of the MLP, and on the right-hand side represents the predicted results of the model. The Mean Square Error (MSE) serves as the loss function during the training process of the MLP and is defined as:

$$MLP_{loss} = \frac{1}{3 \times N} \sum_{i=1}^{N} \left[\left(u_i^t - u_i^p \right)^2 + \left(p_i^t - p_i^p \right)^2 + \left(v_i^t - v_i^p \right)^2 \right]$$
 (5)

In the above formula, u_i^t and u_i^p represents the ground-truth and predicted values of u-velocity, respectively. Similarly, v_i^t , v_i^p and p_i^t , p_i^p denotes the ground-truth and predicted values of v-velocity and pressure p, respectively.

3. Flow Field Data Preparation

The airfoil shapes used in the experiment are obtained by perturbing the CST (Class/Shape Transformation) parameters of the NACA0012 airfoil. CST parameterization method was proposed by Kulfan et al. [14] in 2008. This method primarily describes the geometric shape of an airfoil using a class function and a shape function. It can be represented mathematically as:

$$\zeta(\phi) = C_{N2}^{N1}(\phi)S(\phi) + \phi\zeta_{TE} \tag{6}$$

In the above formula, $\zeta=y/c, \phi=x/c$. Here, c represents the chord length, x and y denotes the airfoil profile's horizontal and vertical coordinates respectively, and ζ_{TE} stands for the airfoil's trailing-edge thickness. The class function can be further represented as :

$$C_{N2}^{N1}(\phi) = \phi^{N1}(1 - \phi)^{N2} \tag{7}$$

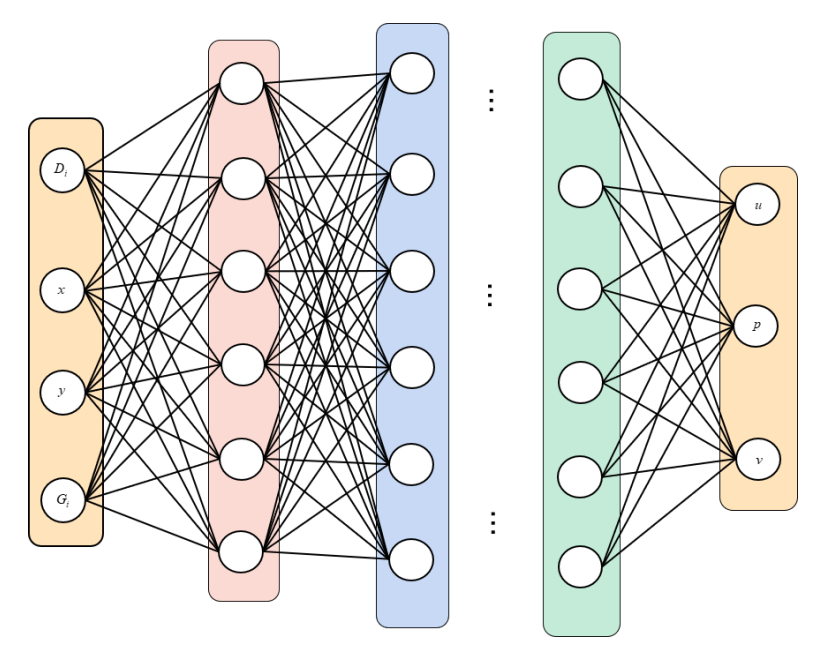


Figure 3 – Neural network architecture for flow field prediction.

For airfoils with a rounded leading edge and a pointed trailing edge, the parameters in the class function are typically $N_1 = 0.5$ and $N_2 = 1.0$. The shape function is represented using an N-th order Bernstein polynomial:

$$S(\phi) = \sum_{i=0}^{N} A_i \left[\frac{N!}{i!(N-i)!} \phi^i (1-\phi)^{N-i} \right]$$
 (8)

In the above formula, N represents the polynomial order, and A_i is an undetermined coefficient. Once A_i is determined, the entire airfoil is defined. As shown in Figure 4, by setting different parameters, a total of 500 airfoils were generated for subsequent flow field prediction tasks.

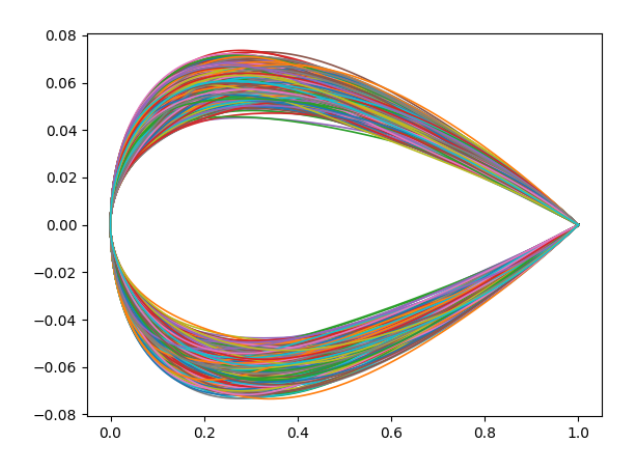


Figure 4 – Multiple airfoils generated by the CST parameterization method.

The flow field modeling work was conducted under the operating conditions of Mach number (Ma) = 0.5, angle of attack (AOA) = 2 $^{\circ}$, and Reynolds number (Re) = 3.0×10^6 . The first grid layer height is set to 8.48×10^{-6} , the computational domain is 364×120 . The turbulence model utilized is the Spalart-Allmaras (SA) model, and the calculations is performed using the PHengLEI software developed by the China Aerodynamics Research and Development Center (CARDC). Using Latin Hypercube Sampling (LHS), 10% of the computed 500 airfoil flow field is selected as the test set, another 10% were designated for cross-validation, and the remaining data served as the training set for the DAN (Deep Attention Network) model. Furthermore, to explore the impact of the Region of Interest (ROI) within the flow field on the prediction effects of the deep learning model, training was

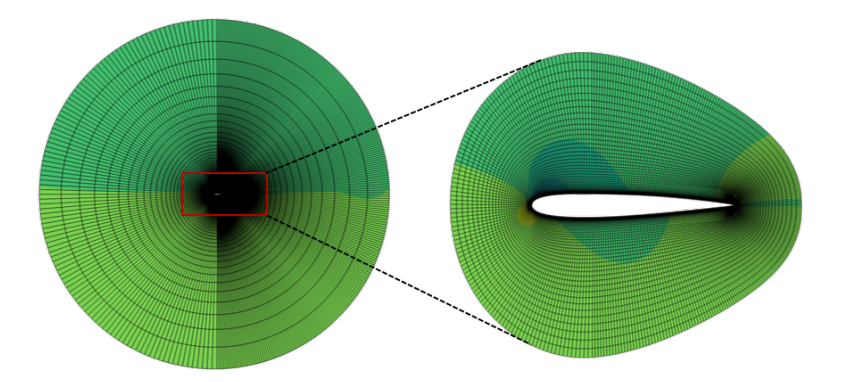


Figure 5 – Flow field mesh dataset. Left: Full-flow data. Right: ROI-Flow data.

conducted separately using two sets: the entire flow field data (Full-Flow) and only the boundary airfoil flow field data (ROI-Flow). The division of the flow field regions is illustrated in Figure 5.

4. Training of the Deep Attention Network Model

During the model training, the initial learning rate was set to 5.0×10^{-5} . The model parameters were trained using the Adam optimizer, and the model underwent 200 iterations. The software and hardware configurations during the model's training, along with the predicted flow field data, are detailed in Table 1. Both the training and testing tasks of the model were completed on a Linux platform, utilizing the NVIDIA RTX 3090 GPU for accelerated training of the deep learning model. For the two types of flow field data (Full-Flow, ROI-Flow), three different MLP neural network architectures (MLP-Nodes-240, MLP-Nodes-300, MLP-Nodes-360) are tested. The detailed settings of the network architectures are shown in the last column of Table 1, where the first number represents the number of network layers, and the second number denotes the number of neurons per layer in the neural network. The loss function curves during the training process for different neural network models are depicted in Figure 6. It can be observed that when using all the flow field data for model training, the model's loss function curves on both the training and cross-validation sets exhibit significant oscillations and converge to relatively high loss values. If modeling is solely focused on the near-wall region (ROI area) of the flow field, a smaller loss is obtained. This suggests that when modeling the entire airfoil flow field, the flow field data from the far field of the airfoil can be considered as noise or dirty data interfering with the neural network's flow field prediction results. By excluding some of the far-field flow field data, the prediction accuracy of the neural network is significantly enhanced. Furthermore, the impact of differences in the number of nodes per layer in the neural network on flow field prediction accuracy is further tested. From Figure 6 and Table 2, it's evident that with an increase in the number of neurons, the Mean Squared Error (MSE) loss of the Deep Attention Network decreases. Specifically, when considering 360 neurons per layer, the MSE loss reduces to 6.48×10^{-6} on the training dataset and 3.31×10^{-4} on the cross-validation set. After comparison, this study sets the number of network layers to 10, each containing 360 neurons, for the subsequent tasks involving the prediction of flow fields in variable-geometry airfoils.

5. Results and Discussion

Firstly, encode the 500 airfoil flow field data obtained in Section III, where airfoil-CST-i(i=1,2,3,...,500). Secondly, validate the flow field prediction capability of the DAN model using the flow field data from the test dataset. To comprehensively investigate the model's generalization, here we select the flow field data labeled as airfoil-CST-19 and airfoil-CST-215 (detailed prediction results can be found in Appendix A) for the testing task of the DAN model. Additionally, for ease of subsequent analysis of flow field test results, the DAN model trained using Full-Flow data will be defined as Full-Flow-DAN, while the one trained using ROI flow field data will be defined as ROI-Flow-DAN. As shown in Figure 7, the predicted results of the test flow field airfoil-CST-19 by both the Full-Flow-DAN and ROI-Flow-DAN models are presented. It's noticeable that when all the flow field data is used for deep learning model training, the flow field curve predicted by Full-Flow-DAN is not smooth and exhibits significant discrepancies from the ground-truth flow field data. Conversely,

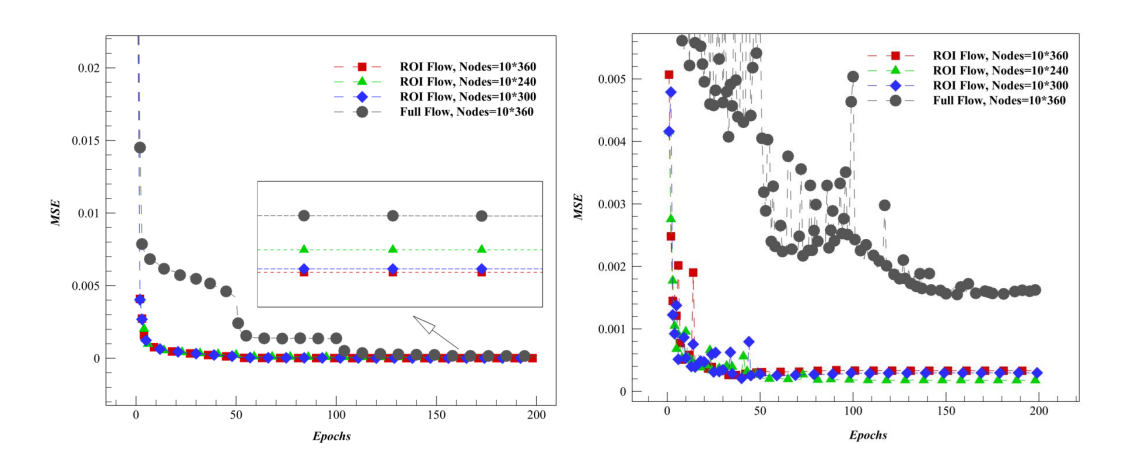


Figure 6 – Loss Function Variation Curve for Training and Validation Sets. Left: Training set. Right: Validation set.

Table 1 – Software and hardware configuration of DAN training

Name	Version	ROI-Flow	Full-Flow	Neural network model
CPU	Intel Xeon Platinum 8273CL	N/A	N/A	N/A
GPU	NVIDIA RTX3090	N/A	N/A	N/A
PyTorch	1.11.0+cu113	N/A	N/A	N/A
Learning rate	5×10^{-5}	N/A	N/A	N/A
Epoch	200	N/A	N/A	N/A
Tensorboard	2.8.0	N/A	N/A	N/A
Computational domain	N/A	364×75	364×120	N/A
MLP-Nodes-360	N/A	\checkmark	\checkmark	10×360
MLP-Nodes-300	N/A	\checkmark	\checkmark	10×300
MLP-Nodes-240	N/A	\checkmark	\checkmark	10×240

Table 2 – Loss of Neural Network Models on Training and Validation Sets

Name	Network archit	ecture	Training set loss	Cross-validation set loss
Full-Flow	MLP-Nodes-360	10×360	1.55×10^{-4}	1.59×10^{-3}
	MLP-Nodes-300	10×300	1.60×10^{-5}	2.97×10^{-4}
ROI-Flow	MLP-Nodes-240	10×240	7.09×10^{-5}	1.77×10^{-4}
	MLP-Nodes-360	10×360	6.48×10^{-6}	3.31×10^{-4}

Table 3 – MAE loss comparison on training and test sets

Model name	$MAE_{u-velocity}$	$MAE_{v-velocity}$	MAE_p
Full-FLow-DAN	0.0159	0.0066	0.0047
ROI-Flow-DAN	0.0093	0.0063	0.0058

the predictions by the ROI-Flow-DAN model demonstrate similarity to the CFD computed results, with a high smoothness in the curve, effectively predicting CFD-computed flow field data. The prediction error meets the requirements of practical engineering applications.

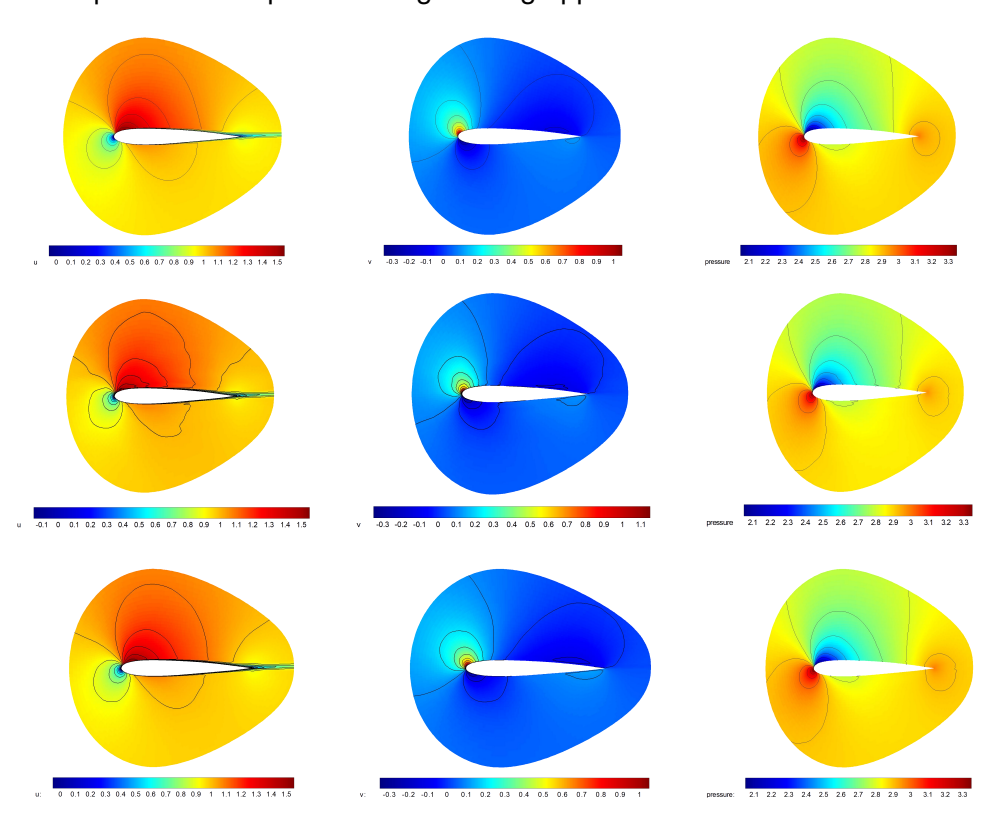


Figure 7 – Comparison diagrams of Airfoil - CST - 19 flow fields. (First row: ground-truth flow fields. Second row: predicted results based on the Full-Flow-DAN model (u-velocity, v-velocity, p). Third row: predicted flow fields of the ROI-Flow-DAN model.)

To visually illustrate the prediction errors of the two models, Figure 8 presents the absolute error contours for the two models regarding test flow field airfoil - CST - 19. The test results reveal that the prediction error of the Full-Flow-DAN model is significantly greater than that of the ROI-Flow-DAN model. For the u-velocity, the maximum error in the prediction results of the Full-Flow-DAN model is 0.32, whereas the maximum absolute error in the prediction of the ROI-Flow-DAN model is only 0.1. Regarding the v-velocity, the maximum absolute error in the Full-Flow-DAN reaches 0.13, while the maximum absolute error in the ROI-Flow-DAN model is only 0.07.

For a more intuitive comparison of the prediction results between the two models, Table 3 presents

the Mean Absolute Error (MAE) values for the prediction results of Full-Flow-DAN and ROI-Flow-DAN models. The MAE is computed using the following formula:

$$MAE = \frac{1}{m} \sum_{i=1}^{m} |(y_i - \hat{y}_i)|$$
 (9)

In the above formula, m represents the number of grid points in the flow field, y_i represents the ground-truth flow field values, and \hat{y}_i represents the predicted flow field values. From the test results in Table 3, it can be observed that training deep learning models using near-wall flow field data effectively enhances the accuracy of flow field predictions. Specifically, for the velocity component v - velocity, the MAE error value of the ROI-Flow-DAN model is reduced by 0.0066 compared to the prediction error of the Full-Flow-DAN model.

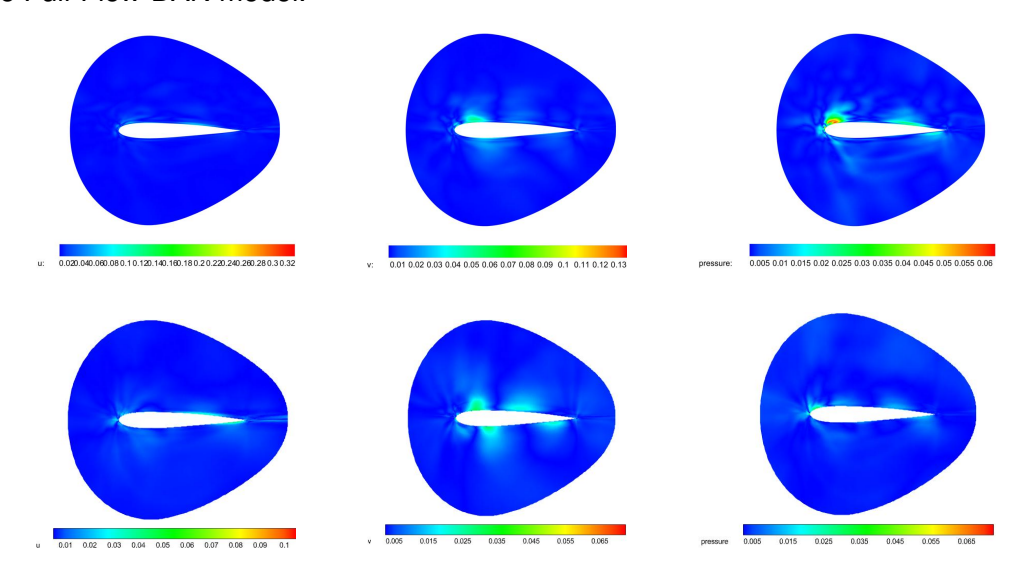


Figure 8 – Airfoil flow field absolute error comparative diagrams. (First row: absolute error diagrams between the predicted results by the ROI-Flow-DAN model and the CFD computed flow fields. Second row: absolute error diagrams between the prediction results by the Full-Flow-DAN model and the ground truth values.)

Figure 9 further provides a comparative analysis between the Full-Flow-DAN and ROI-Flow-DAN models regarding the predicted Cp (pressure coefficient) on the airfoil surface. From the Cp distribution curves shown in Figure 9(a) and Figure 9(b), it's apparent that compared to the Cp prediction curve of the Full-Flow-DAN model, the Cp distribution obtained by the ROI-Flow-DAN model exhibits a better fit with the ground-truth Cp distribution on the airfoil surface. To further illustrate the differences in errors between the two models, Figure 9(c) to Figure 9(f) present histograms and scatter plots of the absolute errors between predicted and ground-truth. In Figure 9(c) and Figure 9(d), it can be observed that the absolute errors of the Cp values predicted by the ROI-Flow-DAN model are more concentrated within the range below 0.04, whereas the absolute errors in the predictions of the Full-Flow-DAN model are more dispersed, especially with numerous errors falling within the range of 0.08. Figure 9(e) and Figure 9(f) provide a clearer visualization of the differences in the distribution of absolute errors between the two models.

To further validate the prediction accuracy of the proposed DAN model for two-dimensional airfoil flow fields, Figure 10(a) presents the velocity profiles predicted by the Full-Flow-DAN model. Three velocity profiles at different stations were chosen to compare the model's prediction results with the ground-truth values. From Figure 10(a), it can be observed that the model's predicted curves closely align with the ground-truth curves. However, there are instances of curvature in the predicted curves at some positions for the first and second stations, especially noticeable at the third station, where the model's predicted curve deviates from the ground truth. For a more intuitive understanding of these error distributions, Figure 10(b) depicts the data distribution histograms of the velocity profiles predicted by the Full-Flow-DAN model at three different stations. It's noticeable that, except for certain positions showing discrepancies, the most data distribution is similar.

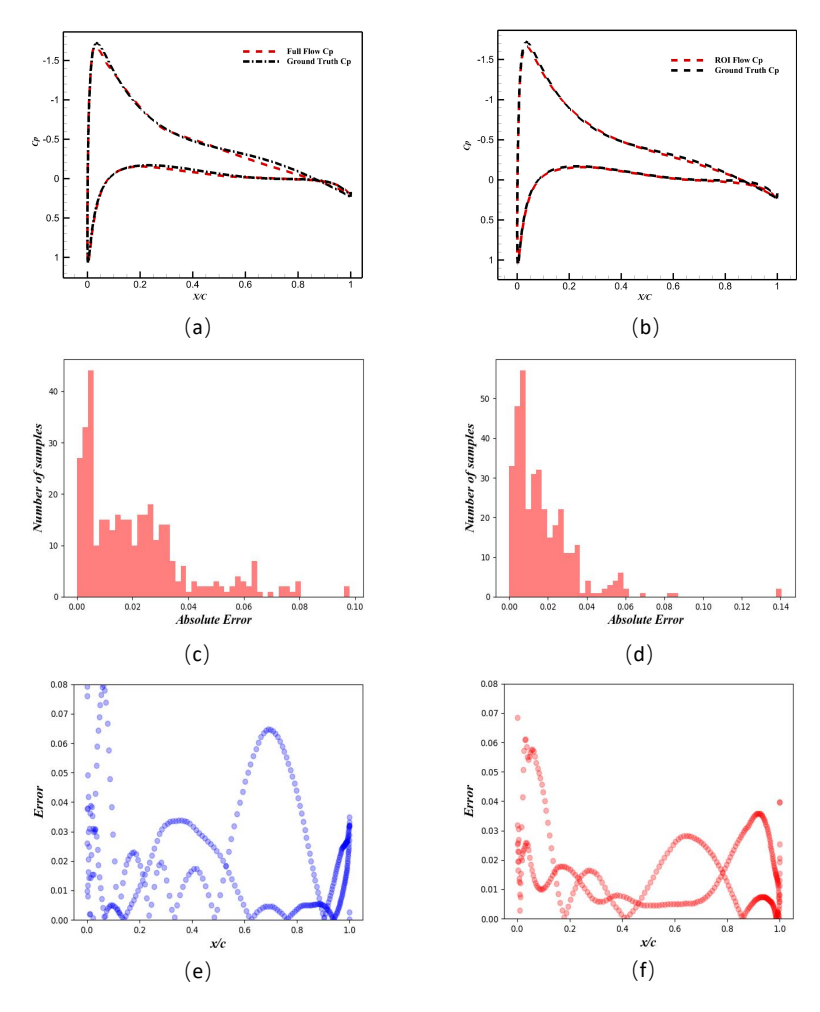


Figure 9 – Airfoil surface Cp distribution curve and absolute error distribution. First row: Cp distribution curve. Second row: absolute error distribution histogram. Third row: scatter plot of absolute error distribution.

Further analysis from the absolute error distribution histograms in Figure 10(c) reveals that the absolute error values predicted by the model at the three different stations are predominantly distributed within 0.05. There are fewer error points at positions further along the x-axis. The maximum error occurs at the first station, with an error value of 0.2.

Figure 11(a) presents the fitting situation of the velocity profiles predicted by the ROI-Flow-DAN model for three different stations compared with the ground-truth velocity curves. These three test stations are the same as those presented in Figure 10. It can be observed that compared to the predictions of the Full-Flow-DAN model, the ROI-Flow-DAN model shows a better fit between the predicted velocity curve and the ground-truth velocity curve, without similar curve transition issues.

From the histogram in Figure 11(b), it can be seen that at the first station, the predicted data distribution by the ROI-Flow-DAN model is closely aligned with the ground truth data distribution, while there is some error at the second and third stations. Further observation of the histogram of absolute errors reveals that the absolute errors at the first and second stations are roughly distributed within 0.01, with the largest error occurring at the third station, with a value of 0.03. This value is significantly lower compared to the maximum error of 0.2 obtained by the Full-Flow-DAN model, further illustrating that the ROI-Flow-DAN model achieves more precise prediction results than the Full-Flow-DAN model.

6. Conclusion

To enhance the efficiency of flow field modeling, this paper introduces a novel deep attention network for rapid prediction of 2D airfoil flow fields. To improve the interpretability of airfoil geometric features, different airfoil geometric features were extracted using a Transformer encoder. The encoded

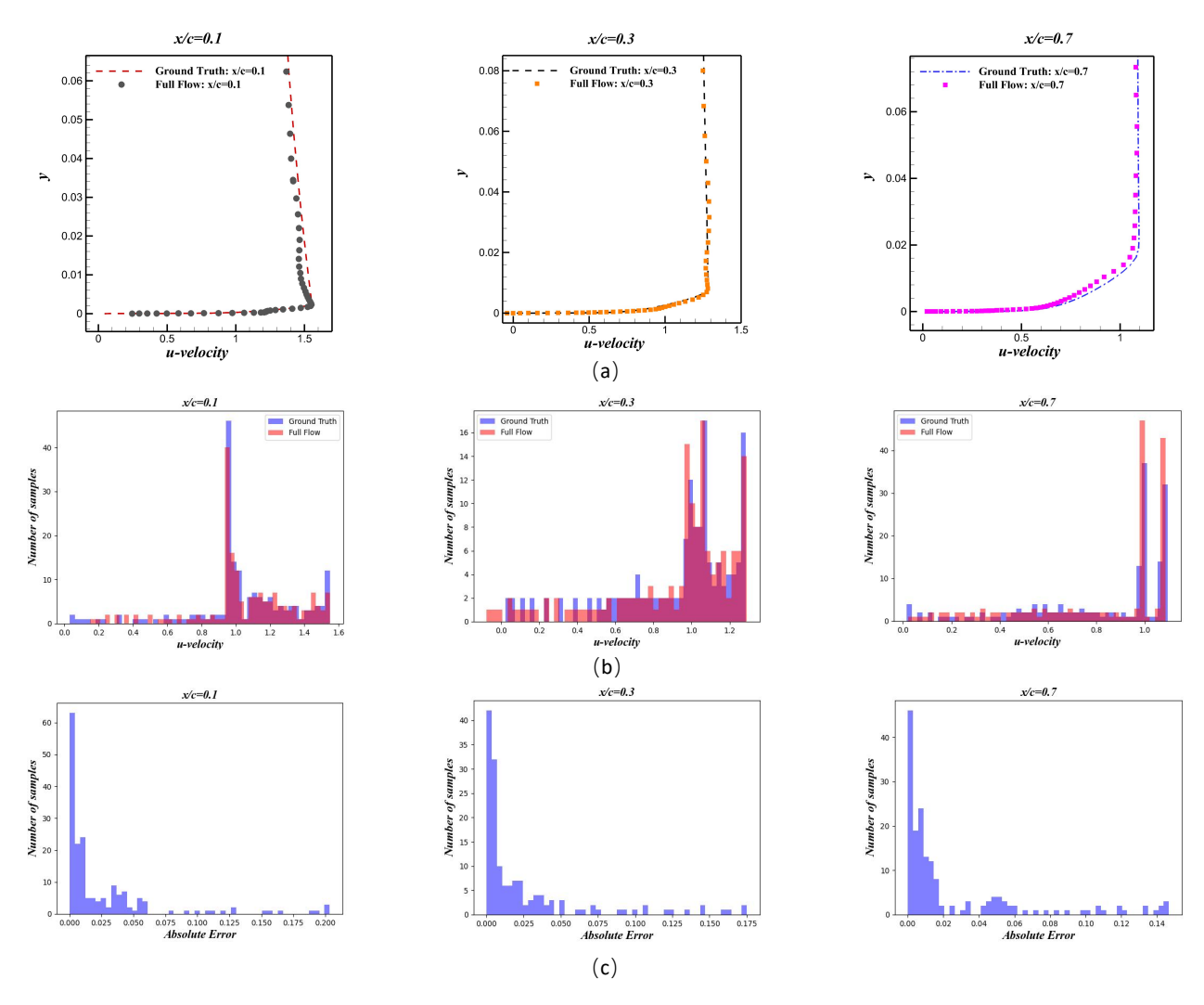


Figure 10 – Fitting curves of velocity profiles at different locations and histograms of data distributions. ((a) Fitted curves of velocity profiles at three different locations. (b) Histograms of the ground truth and predicted velocity values at different locations. (c) Histogram depicting the distribution of absolute errors between predicted and ground truth velocity values at different locations.)

airfoil geometric features were evenly distributed across the near-wall region of the two-dimensional airfoil. Compared to convolutional neural networks, this approach exhibits greater interpretability. Experimental results further validate the excellent generalization of this method in extracting airfoil geometric features. Furthermore, the airfoil geometric features extracted by the Transformer encoder were associated and encoded with the flow field's wall distance and coordinates. These features were fed into a MLP to predict the velocity and pressure fields of the airfoils. A comparison between the Full-Flow-DAN and ROI-Flow-DAN models regarding prediction accuracy revealed that ROI-Flow-DAN achieved superior accuracy with a maximum MAE value of only 0.0093. This highlights that training the model using near-wall flow field data significantly enhances the predictive accuracy of deep learning models. In future work, we aim to further explore this method's applicability in the rapid prediction of three-dimensional flow fields. Additionally, by incorporating relevant physical constraints, it aims to enhance both the physical interpretability and generalization of the deep learning flow field modeling.

7. Contact Author Email Address

The corresponding author email address is aeroelastic@nwpu.edu.cn (Weiwei Zhang) or you can contact with the email address with zuokuijun13@163.com (Kuijun Zuo) and yuanxianxu@cardc.cn (Xianxu Yuan).

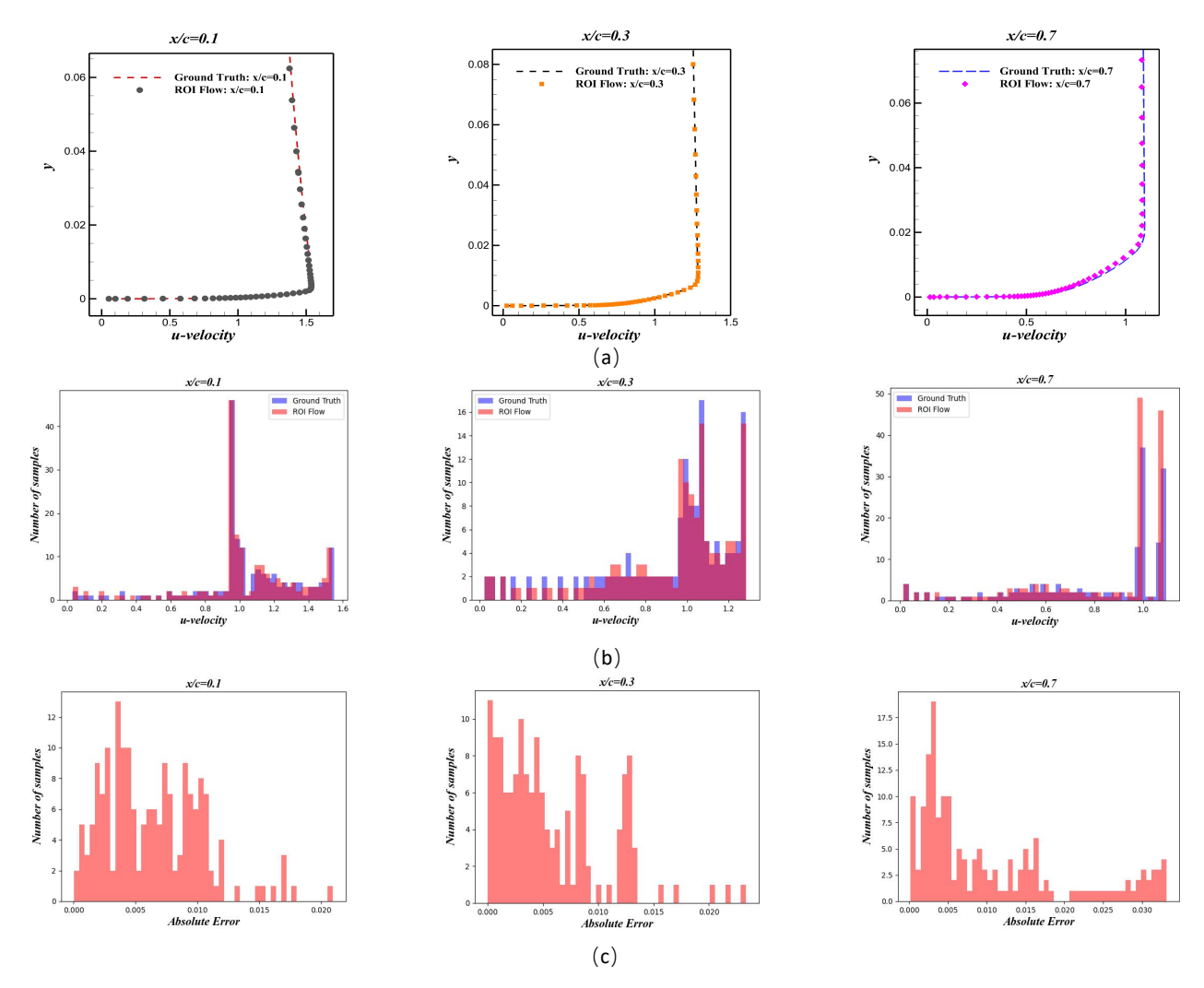


Figure 11 – Fitting curves of velocity profiles at different locations and histograms of data distributions. ((a) Fitted curves of velocity profiles at three different locations. (b) Histograms of the ground truth and predicted velocity values at different locations. (c) Histogram depicting the distribution of absolute errors between predicted and ground truth velocity values at different locations.)

8. Copyright Statement

The authors confirm that they, and/or their company or organization, hold copyright on all of the original material included in this paper. The authors also confirm that they have obtained permission, from the copyright holder of any third party material included in this paper, to publish it as part of their paper. The authors confirm that they give permission, or have obtained permission from the copyright holder of this paper, for the publication and distribution of this paper as part of the ICAS proceedings or as individual off-prints from the proceedings.

References

- [1] Guo X, Li W, Iorio F. Convolutional neural networks for steady flow approximation. *Proceedings of the 22nd ACM SIGKDD international conference on knowledge discovery and data mining*, pp 481-490, 2016.
- [2] Duru C, Alemdar H, Baran Ö U. CNNFOIL: convolutional encoder decoder modeling for pressure fields around airfoils. *Neural Computing and Applications*, Vol. 33, No. 12, pp 6835-6849, 2021.
- [3] Dosovitskiy A, Beyer L, Kolesnikov A, et al. An Image is Worth 16x16 Words: Transformers for Image Recognition at Scale, *International Conference on Learning Representations*, 2020.
- [4] Wu M Y, Wu Y, Yuan X Y, et al. Fast prediction of flow field around airfoils based on deep convolutional neural network. *Applied Sciences*, Vol. 12, No. 23, pp 12075, 2022.
- [5] Ribeiro M D, Rehman A, Ahmed S, et al. DeepCFD: Efficient steady-state laminar flow approximation with deep convolutional neural networks. *arXiv* preprint *arXiv*: 2004.08826, 2020.

- [6] Chen D, Gao X, Xu C, et al. FlowGAN: A conditional generative adversarial network for flow prediction in various conditions. *2020 IEEE 32nd International Conference on Tools with Artificial Intelligence (ICTAI)*, pp 315-322, 2020.
- [7] Wu H, Liu X, An W, et al. A deep learning approach for efficiently and accurately evaluating the flow field of supercritical airfoils. *Computers Fluids*, Vol. 198, 2020.
- [8] Wang Z, Liu X, Yu J, et al. A general deep transfer learning framework for predicting the flow field of airfoils with small data. *Computers Fluids*, Vol. 251, 2023.
- [9] Hu J W, Zhang W W. Mesh-Conv: Convolution operator with mesh resolution independence for flow field modeling. *Journal of Computational Physics*, Vol. 452, 2022.
- [10] Sekar V, Jiang Q, Shu C, et al. Fast flow field prediction over airfoils using deep learning approach. *Physics of Fluids*, Vol. 31, No. 5, 2019.
- [11] Zuo K, Bu S, Zhang W, et al. Fast sparse flow field prediction around airfoils via multi-head perceptron based deep learning architecture. *Aerospace Science and Technology*, Vol. 130, 2022.
- [12] Vaswani A, Shazeer N, Parmar N, et al. Attention is all you need. *Advances in neural information processing systems*, Vol. 30, 2017.
- [13] Dosovitskiy A, Beyer L, Kolesnikov A, et al. An image is worth 16x16 words: Transformers for image recognition at scale. *arXiv* preprint *arXiv*: 2010.11929, 2020.
- [14] Kulfan B M. Universal parametric geometry representation method. *Journal of aircraft*, Vol. 45, No. 1, pp 142-158, 2008.

A Appendix: Airfoil-CST-215 Flow Field Prediction Results

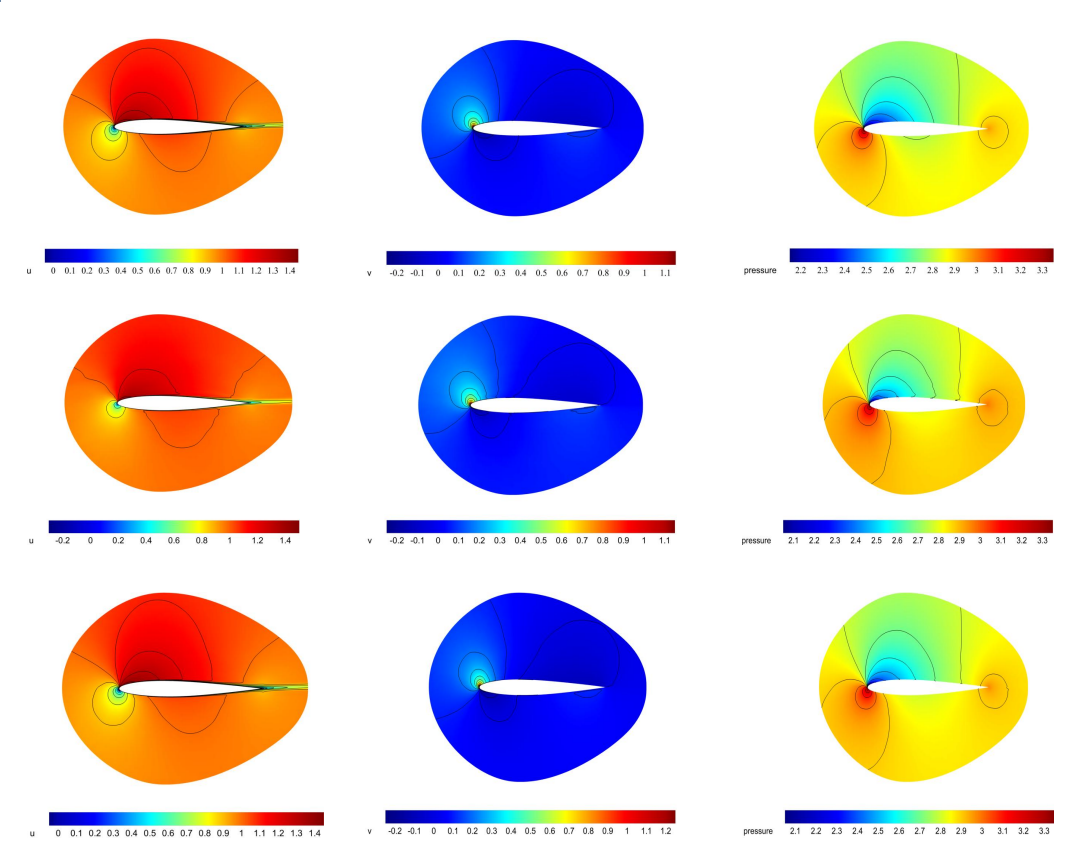


Figure 1 – Comparison diagrams of Airfoil - CST - 215 flow fields. (First row: ground-truth flow fields. Second row: predicted results based on the Full-Flow-DAN model (u-velocity, v-velocity, p). Third row: predicted flow fields of the ROI-Flow-DAN model.)

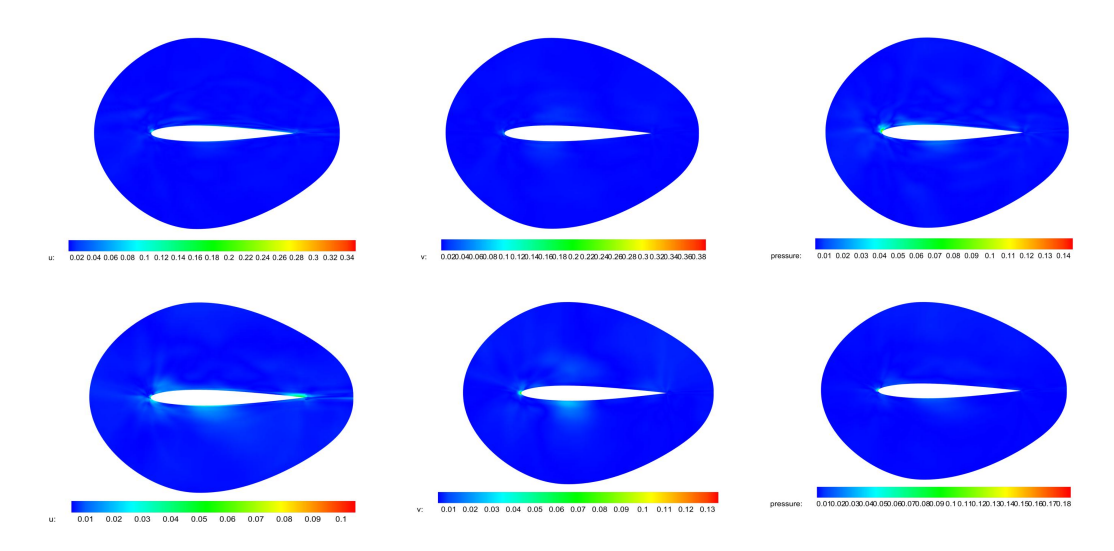


Figure 2 – Airfoil flow field absolute error comparative diagrams. (First row: absolute error diagrams between the predicted results by the ROI-Flow-DAN model and the CFD computed flow fields. Second row: absolute error diagrams between the predicted results by the Full-Flow-DAN model and the ground truth values.)

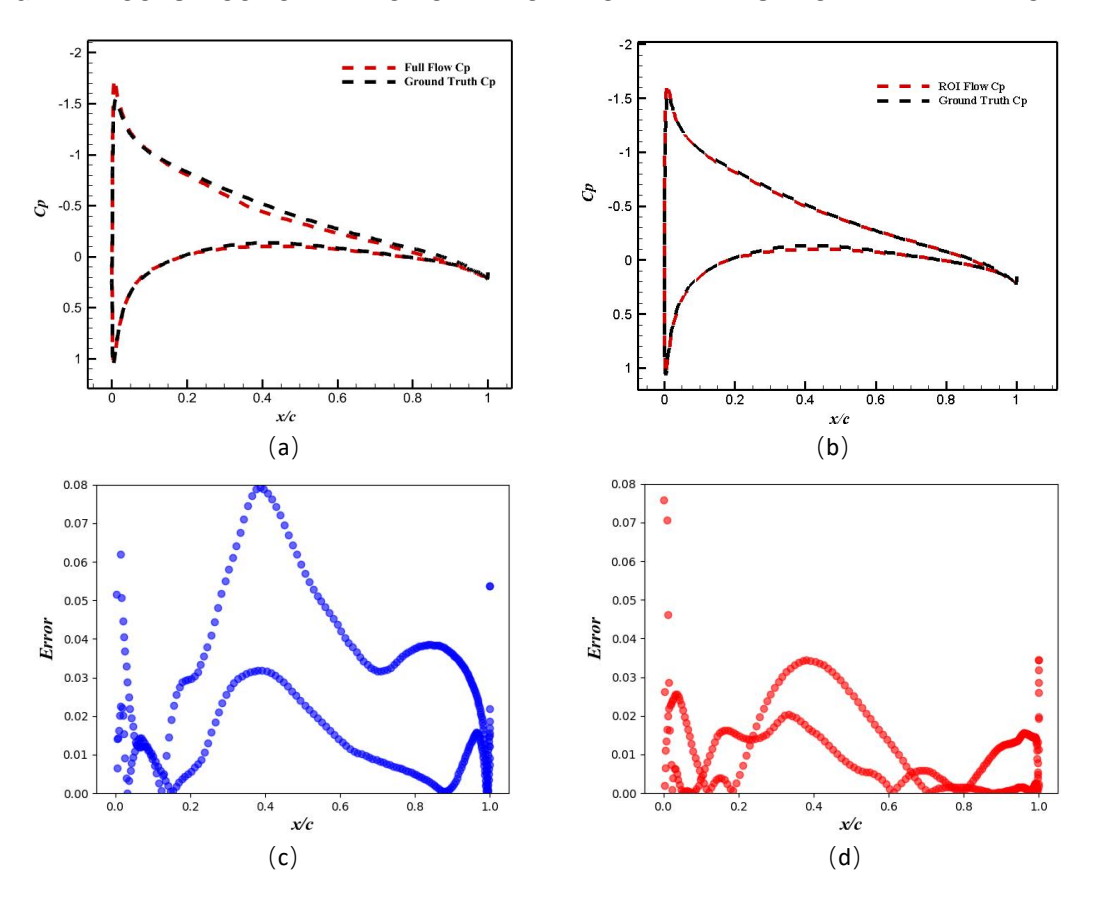


Figure 3 – Airfoil surface Cp distribution curves and absolute error distribution scatter plots.

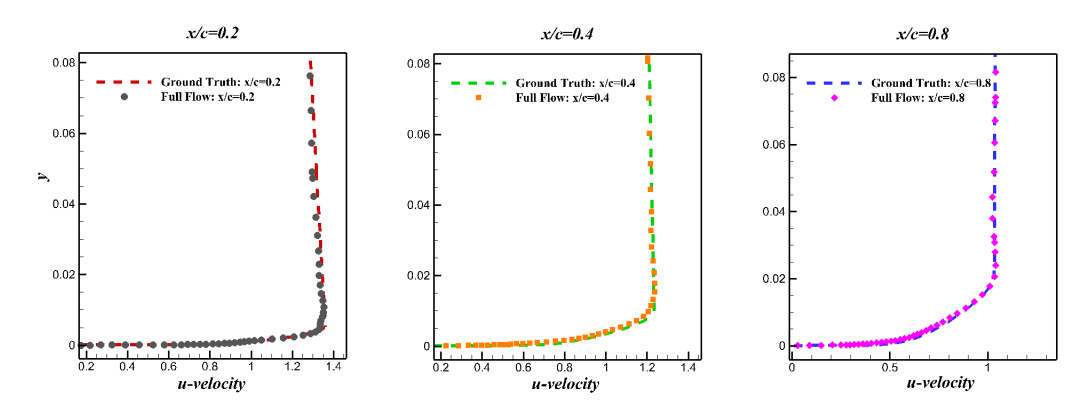


Figure 4 – Velocity fitting curves of predicted and ground truth values at three different station points for the Full-Flow-DAN model.

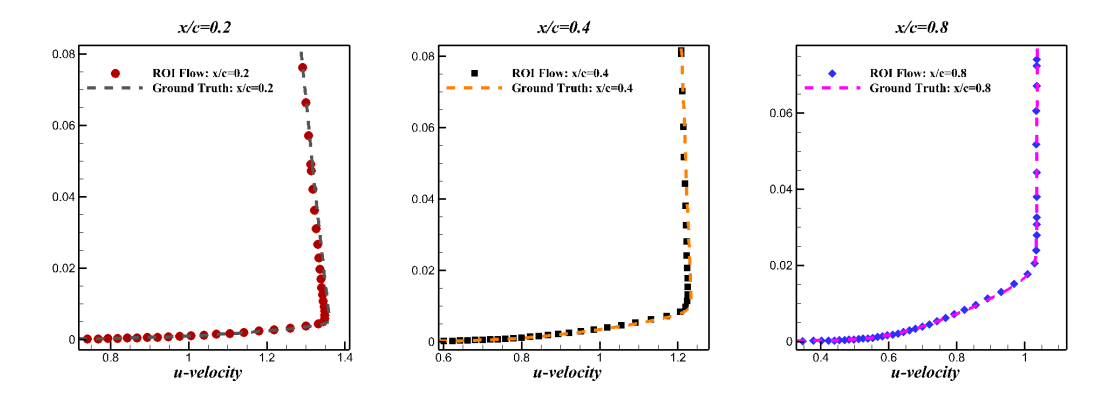


Figure 5 – Velocity fitting curves of predicted and ground truth values at three different station points for the ROI-Flow-DAN model.